HHS Public Access

Author manuscript

J Comput Neurosci. Author manuscript; available in PMC 2020 December 01.

Published in final edited form as:

J Comput Neurosci. 2019 December ; 47(2-3): 109–124. doi:10.1007/s10827-019-00727-3.

A Novel Neural Computational Model of Generalized Periodic Discharges in Acute Hepatic Encephalopathy

Jiang-Ling Song,
The Medical Big Data Research Center, Northwest University, Xi'an, China 710127 and the Department of Neurology, Massachusetts General Hospital, Boston, MA

Luis Paixao,
The Department of Neurology, Massachusetts General Hospital, Boston, MA

Qiang Li,
The Medical Big Data Research Center, Northwest University, Xi'an, China 710127

Si-Hui Li,
The Medical Big Data Research Center, Northwest University, Xi'an, China 710127

Rui Zhang,
The Medical Big Data Research Center, Northwest University, Xi'an, China 710127

M. Brandon Westover*
The Department of Neurology, Massachusetts General Hospital, Boston, MA

Abstract

Acute hepatic encephalopathy (AHE) due to acute liver failure is a common form of delirium, a state of confusion, impaired attention, and decreased arousal. The electroencephalogram (EEG) in AHE often exhibits a striking abnormal pattern of brain activity, which epileptiform discharges repeat in a regular repeating pattern. This pattern is known as generalized periodic discharges, or triphasic-waves (TPWs). While much is known about the neurophysiological mechanisms underlying AHE, how these mechanisms relate to TPWs is poorly understood. In order to develop hypotheses how TPWs arise, our work builds a computational model of AHE (AHE-CM), based on three modifications of the well-studied Liley model which emulate mechanisms believed central to brain dysfunction in AHE: increased neuronal excitability, impaired synaptic transmission, and enhanced postsynaptic inhibition. To relate our AHE-CM to clinical EEG data from patients with AHE, we design a model parameter optimization method based on particle filtering (PF-POM). Based on results from 7 AHE patients, we find that the proposed AHE-CM not only performs well in reproducing important aspects of the EEG, namely the periodicity of triphasic waves (TPWs), but is also helpful in suggesting mechanisms underlying variation in EEG patterns seen in AHE. In particular, our model helps explain what conditions lead to increased

*corresponding author. M. Brandon Westover, mwestover@mgh.harvard.edu.

frequency of TPWs. In this way, our model represents a starting point for exploring the underlying mechanisms of brain dynamics in delirium by relating microscopic mechanisms to EEG patterns.

Keywords

Acute hepatic encephalopathy (AHE); Neural computational model; Liley model; Generalized periodic discharges; Electroencephalogram (EEG); Particle filtering

1 Introduction

Acute hepatic encephalopathy (AHE) is a common condition, occurring in 30-45% of cirrhotic patients [1]. AHE is associated with decreased quality of life, increased hospitalization and increased mortality [2]. It is defined as a reversible clinical syndrome of impaired brain function occurring in patients with acute liver failure (ALF), and clinically leads to impaired attention, confusion and decreased arousal[3]. Many patients with AHE exhibit a strikingly abnormal pattern of brain activity in the electroencephalogram (EEG), in which epileptiform discharges repeat in a regular repeating pattern. This pattern is known as generalized periodic discharges [4], or triphasic-waves (TPWs) [5].

Neural computational modeling is a well-established and rapidly increasing research area, which has been successfully applied to the biomedical field to analyze and understand the observed EEG phenomena, test mechanistic hypotheses, and predict system behaviors in space and/or time [6]. Various computational models have been developed to simulate neuronal dynamics and shed light on the mechanisms underlying EEG patterns in healthy and pathological states, including epilepsy, sleep disorders, and other neurological conditions. These neural computational models can be categorized into two main families according to the level of biological organization they aim to represent: microscopic model and mesoscopic model. The former one describes interconnected neurons with each single neuron represented in detail by multiple compartments to model their structural components and functional properties [7,8,9,10,11]. Although such models can reflect brain dynamics more realistically, they are challenging to implement on a large scale due to the high computational cost and complexity. In contrast, mesoscopic models study spatially averaged activity to characterize the collective behavior of neural populations instead of modeling the dynamic properties of individual neurons [12,13,14,15,16,17,18]. Since mesoscopic models are able to capture certain brain dynamics in a simple and biologically explanative way, there has been increasing interest in the study of mesoscopic models to explore physiological or pathological phenomenon.

In 1952, Beurle modelled the cortex as a spatially uniform and continuous network with a fixed firing threshold [8], which broke new ground in characterizing brain dynamics from the “neural population” point of view. This work allowed researchers to more effectively tackle important and clinically-relevant open questions in neuroscience, including the origin of oscillations in the mammalian EEGs [7], including the alpha (8-13 Hz) rhythm [9][19] and EEG patterns during epileptic seizures in the olfactory system [20], among others. However, these early computational models had a number of limitations, such as (1) inaccurate representation of the postsynaptic response; (2) poorly defined neural sub-

populatio (3) incomplete local or global connectivity; and (4) difficulties in obtaining independent estimates of model parameters [21]. In an effort to overcome some of these limitations, a variety of improved computational models have been developed. Among these, the model proposed by Liley in 1997 has been successful in clarifying the genesis of alpha rhythms in the mammalian brain [21]. In this model, two neural populations (excitatory and inhibitory) are connected via local feedforward and feedback excitatory and inhibitory couplings, and synaptic reversal potentials are incorporated in each population so that conductance-based neurons are defined. In [22], Liley et al. further proposed an improved form of this model with more generalized mathematical formulations which could be applied if the proposed nine assumptions were achieved. For convenience, we refer to this model as the "Liley model" in what follows.

Recent work on patients with anoxic brain injury has shown that a modification of the Liley model can reproduce generalized periodic discharges, which are similar to the TPW EEG patterns seen in AHE patients [23]. Building on this work, we study a modified Liley model in order to relate observed EEG patterns (TPWs) to mechanisms believed to be important in generating the neurological manifestations of delirium in AHE. To achieve this goal, a new computational model of AHE (AHE-CM) will be first proposed by integrating three known mechanisms underlying AHE into the Liley model: (1) impaired synaptic transmission secondary to impaired cellular metabolism; (2) increased neuronal excitability; and (3) enhanced postsynaptic inhibition. Then, to match this model to features of actual EEGs from patients with AHE, a parameter optimization method based on particle filtering (PF-POM) will be designed. In this work, we focus specifically on tuning the model to approximately reproduce the distribution of inter-TPW intervals. Finally, through combining AHE-CM with PF-POM, we study the model behaviours in response to changes in key parameters, as well as the relation between the frequency of TPWs in real AHE-EEGs and the mechanisms underlying AHE in our computational model. Performance of the proposed model will be verified on seven AHE patients hospitalized at Massachusetts General Hospital (MGH).

This paper is organized as follows. In section II, we introduce the proposed approach, including the neural computational model of AHE (AHE-CM) together with the mechanisms underlying AHE, and the model parameter optimization method PF-POM. In section III, we analyze the model performance on EEGs from 7 patients who were hospitalized at the Massachusetts General Hospital.

2 Methods

This section introduces our neural computational model of AHE (AHE-CM), and a model parameter optimization method based on particle filtering (PF-POM).

2.1 Neural computational model of AHE

In this subsection, we first give a brief overview of "Liley model", including its topological structure and the dynamics of each neural population. Then we summarize three key neuropathological alterations believed to underlie delirium in AHE. Finally, a new neural computational model of AHE (AHE-CM) is proposed by integrating the three mechanisms into the Liley model.

A1) Overview of the Liley model—The Liley model comprises two neural populations: an excitatory population (represented by **E**) and an inhibitory population (represented by **I**), which are functionally distinct but synaptically coupled. The model includes two inter-connections (weighted by N_{ie} and N_{ei}) and two intra-connections (weighted by N_{ee} and N_{ii}). External input from thalamus to **E** and **I** are presented by p_{ee} and p_{ei}. Fig. 1 illustrates the topological structure.

The dynamics of each population are described by two state variables, the soma membrane potential and the post-synaptic potential. The soma membrane potential V is modeled according to conductance-based rules [24], specifically,

$$\tau \dot{V}(x,t) = V^r - V(x,t) + \sum \psi(V(x,t)) I(x,t) \tag{1}$$

where

$$\psi(V(x,t)) = \frac{[V^{eq} - V(x,t)]}{\mid V^{eq} - V^r \mid}. \tag{2}$$

Here, V^r is the resting membrane potential and V^{eq} represents the reversal potential. On the other hand, post-synaptic potential I is modeled according to the convolution-based rules, specifically,

$$I(x,t) = h(t) \otimes m(x,t) \tag{3}$$

where

$$\begin{aligned} m(x,t) &= S(V(x,t)) \\ &= \frac{Q^{max}}{1 + e^{-\sqrt{2}(V(x,t) - V_0)/\sigma}}, \end{aligned} \tag{4}$$

$$h(t) = \Gamma \gamma t e^{1-\gamma t} (t \geq 0). \tag{5}$$

Note that $m(x, t)$ and $h(t)$ denote the firing rate and impulse response of a population where t represents time and x corresponds to the spatial position of the population in the brain. In (4), $S(\cdot)$ is a sigmoid function, Q_{max} is the maximum population firing rate, σ is the steepness of the sigmoidal transformation, and V_0 is firing threshold. In (5), Γ represents the peak amplitude of the post-synaptic potential and γ characterizes the exponential decay time scale of the post-synaptic potential. For convenience in calculating the convolution ($\otimes$ in (3), further taking the Laplace transformation on it, then Eq. (3) can be re-expressed by a non-linear partial differential equation as

$$\ddot{I}(x,t) = -2\gamma \dot{I}(x,t) - \gamma^2 I(x,t) + \Gamma \gamma e \cdot m(x,t). \tag{6}$$

Details of the transformations of electrical activities in the Liley model are shown in Fig.2. Blue lines represent intra-connected loops and the green dotted lines represent inter-connected loops. In each loop, the post-synaptic potential I can be obtained from the soma membrane potential V by Eq. (3), which is completed by two computational blocks (see sub-figure in Fig. 2): a potential-to-rate block (represented by "S") and a rate-to-potential block (represented by "h"). Specifically, the soma membrane potentials V is transformed into firing rate m by Eq. (4) in the first block, and the firing rate m is converted into the post-synaptic potential I by Eq. (5) in the second block. After that, the post-synaptic potential I is further transferred into the soma membrane potential V according to Eqs. (1)-(2).

A2) Neuropathological alterations of AHE—In acute liver failure, there is a systemic build-up of toxic substances from the gut, including ammonia, that are normally metabolized and excreted by the liver [3]. These toxins travel via the bloodstream to the brain, ultimately leading to development of AHE. Among numerous cellular and neurophysiological mechanisms underlying AHE, we we focus here on three for which there is clear evidence for a role in development of AHE. These are (1) impaired synaptic transmission secondary to reduced cellular metabolism; (2) increased neuronal excitability; and (3) enhanced postsynaptic inhibition.

Brain concentrations of ATP are significantly reduced in experimental animal models of AHE [25][26]. This is thought to result from hyperammonia-induced mitochondrial dysfunction, systemic ischemia and hypoxia and increased ATP consumption [25][27]. The latter process may be secondary to hyperammonia-induced glutamate N-methyl-D-aspartate (NMDA) receptor hyperactivation and concomitant compensatory excessive activation of the sodium/potassium ATPase pump to maintain cellular sodium levels within the normal range [25][27]. Given that synaptic neurotransmission is a highly metabolically expensive process, accounting for 30% of the brain's adenosine triphosphate (ATP) usage [28], it is likely that ATP depletion observed in AHE is associated with impaired synaptic signaling. Supporting this claim, studies have shown that the reduction in brain ATP levels coincides with the onset of AHE-associated behavioral impairment and EEG abnormalities [25][26].

Increased neuronal excitability is another key mechanism underlying AHE. Increased neuronal excitability in AHE appears to arise from two processes: hyperactivation of glutamate NMDA receptors and anoxic long-term potentiation. Ammonia levels are significantly increased in AHE patients [29], and elevated ammonia levels in acute liver failure (ALF) animal models lead to overactivation of NMDA glutamate receptors ([30]). Enhanced NMDA-mediated neuronal excitability is also supported by studies which demonstrate decreased expression of astrocytic glutamate transporters (EAAT-2) [31] and astrocytic glycine transporters (GLYT-1) [14], corresponding to increased levels of synaptic glutamate and glycine, agonists and co-agonists of NMDA receptors respectively, in ALF rat models and AHE patients. The resultant overactivation of glutamate NDMA receptors is followed by excessive formation of nitric oxide and cyclic guanosine monophosphate (cGMP), and ultimately increased neuronal excitability [30]. In addition, anoxic long-term potentiation, the phenomenon of increased excitatory postsynaptic potential (EPSP) amplitudes following exposure to ischemia or anoxia, may also contribute to increased neuronal excitability in AHE. Indeed, AHE is often accompanied by a variety of other

medical processes which may lead to decreased brain oxygenation, such as gastrointestinal bleeding, sepsis, or the effects of cytokines and other toxins released from necrotic liver tissue [32][33].

Finally, a growing body of evidence suggests that enhanced gamma-aminobutyric acid (GABA)- and glycine-mediated postsynaptic inhibition may also be central to the pathophysiology of AHE. Levels of pregnenolone-derived neurosteroids (e.g. allopregnanolone), potent selective positive allosteric modulators of the $GABA_A$ receptor, are significantly increased in experimental ALF models and in brains of hepatic coma patients [34]. Additionally, a study in a rabbit model of ALF has shown greatly increased levels of GABA-like activity in peripheral blood plasma just before the onset of AHE [35]. As with ammonia, this finding may be partially due to impaired hepatic extraction of gut derived GABA from portal venous blood [35]. The same study also showed that the blood-brain barrier becomes abnormally permeable to an isomer of GABA before the onset of AHE, and that hepatic coma is associated with an increase in the brain density of GABA receptors [35], thereby increasing the sensitivity of the brain to GABA-ergic neural inhibition. Another study showed that treatment with flumazenil, a GABA-benzodiazepine receptor antagonist, appears to result in clinical and electroencephalographic improvements in AHE patients [36]. Further, increased levels of synaptic glycine, an inhibitory neurotransmitter observed in AHE, may lead to over-activation of glycine receptors, which together with the hyperactivation of GABA receptors result in post-synaptic inhibition through chloride-channel opening.

A3) Neural computational model of AHE—To begin building our neural computational model of AHE (AHE-CM), we mathematically augment the Liley model to capture the three pathophysiologic mechanisms described above for AHE. We consider only temporal dynamics; we do not model spatio-temporal dynamics in this work.

First, the postsynaptic potential amplitude Γ in Eq. (6) is taken as a variable satisfying the slow dynamics of itself coupled to the presynaptic firing rate $S(\cdot)$ as in the work of Bojak et.al. [37], which can be expressed by

$$\dot{\Gamma}_k(t) = \frac{\Gamma_k^{rest} - \Gamma_k(t)}{\tau_k^{rec}} - p_k^{dep} S(V_e(t)) \Gamma_k(t)\,. \tag{7}$$

Here, p_k^{dep} is the depletion constant reflecting the impaired synaptic transmission, Γ_k^{rest} is the resting value of the maximum amplitude of the postsynaptic potential (PSP), and τ_k^{rec} is the recovery time for activity dependent synaptic depression, subscript $k \in \{e, i\}$ indicate excitatory and inhibitory populations, respectively. Note that this mechanism applies to both excitatory and inhibitory populations.

Next, to model the effect of increased neuronal excitability, we modify the Liley model to amplify the resting value of maximum amplitude Γ^{rest} of the excitatory postsynaptic potential (EPSP) in Eq. (7). This is accomplished by setting,

$$\Gamma_e^{rest} = \Gamma_e^{equ} * (1 + F_{am}) \tag{8}$$

where Γ_e^{equ} is the equilibrium voltage of the EPSP and F_{am} is the amplification factor. This mechanism applies only to the excitatory population.

We last model enhanced postsynaptic inhibition, caused by the increased GABAergic neural transmission. To do this, we prolong the duration of the inhibitory postsynaptic potential (IPSP) by altering the decay rate constant γ_i in Eq. (6) according to [38], so that the inhibitory post-synaptic potential is given by

$$\ddot{I}_i(t) = -(\gamma_i + \tilde{\gamma}_i)\dot{I}_i(t) - \gamma_i\tilde{\gamma}_i I_i(t) + \Gamma(t)\tilde{\gamma}_i e^{\frac{\gamma_i}{\gamma_i^0}} m(t) \tag{9}$$

where

$$\begin{aligned} \gamma_i &= \gamma_i^0 / \lambda_i, \\ \tilde{\gamma}_i &= \rho_i \gamma_i, \\ \lambda_i &= e^{\epsilon_i} - 1 / \epsilon_i, \\ \rho_i &= e^{\epsilon_i}. \end{aligned} \tag{10}$$

Here, γ_i^0 is the baseline synaptic time constant, ϵ_i is the control parameter relating to the decay time of the IPSP. This mechanism applies only to the inhibitory population.

On the basis of the dynamics of each population and detailed transformation of electrical activities in Liley model, the proposed neural computational model of AHE (AHE-CM) can be formulated by combining the mathematical expressions (7)-(9) of three mechanisms. Eq. (11) presents the mathematical model of AHE-CM. The Euler-Maruyama method with a time step of 0.1ms is applied to solve the Eq. (11) and the soma membrane potential of the excitatory population (i.e. V_e) is taken to represent the EEG signal. We denote by Θ the set of parameters in AHE-CM. A detailed explanation of the biological interpretation of these parameters and their default values, which we adopt, can be found in [38].

2.2 Parameter values

In this subsection, we give some illustrations about how to set the newly introduced parameters (F_{am}, γ_i, τ_e^{rec}, τ_i^{rec}) in our work.

Modeling impaired synaptic transmission—To characterize impaired synaptic transmission in AHE, we follow the idea in the bursting Liley model of including synaptic depression [37], which means that the postsynaptic peak amplitudes Γ_e and Γ_i decrease as a function of presynaptic firing rates and recover with time constants τ_e^{rec} and τ_i^{rec} (i.e. Eq.

(7)). We set baseline values of τ_e^{rec} to 500ms and τ_i^{rec} to 250ms, in agreement with the physiological range of 250ms to 1000ms [39]. According to the work of Ruijter et al.[23], the impaired synaptic transmission will induce τ_e^{rec} and τ_i^{rec} that are dramatically increased. Therefore, τ_e^{rec} and τ_i^{rec} are varied from their baseline to their maximum value. When varying these parameters in our experiments, because excitatory synapses are believed to recover more slowly than inhibitory synapses [40], we allow a larger range for τ_e^{rec} [500 20000]ms than for τ_i^{rec} [250 2500]ms, as in [23].

Modeling elevated neuronal excitability and enhanced postsynaptic inhibition —To model the effect of elevated neuronal excitability, we increased the resting value of maximum EPSP (Γ_e^{rest}) through the parameter "F_{am}". Note that, as shown in Eq. (7), Γ_e is reduced because of the impaired synaptic transmission and may recover with time constant τ_e^{rec} to its baseline value. While through the parameter F_{am}, it may increase above its baseline value, reflecting increased neuronal excitability. We set the magnitude order of F_{am} to the same values used in the work of Rujiter et.al [23] in modeling HIE.

To model enhanced gamma-aminobutyric acid and glycine-mediated postsynaptic inhibition, we followed the approach of [38], which modeled effects of anesthesia with $GABA_A$ agonists (e.g. propofol). The baseline value of the synaptic rate constant (γ_i^0) is $0.065ms^{-1}$, which agrees with the physiological range of $0.01ms^{-1}$ to $0.5ms^{-1}$ [23]. The magnitude order of ϵ_i is chosen according to [41]. The postsynaptic potential decay rate γ_i can be calculated by Equation (10).

$$\tau_e \dot{V}_e(x,t) = V_e^{rest} - V_e(x,t) + \psi_{ee}(V_e(x,t))I_{ee}(x,t) + \psi_{ie}(V_e(x,t))I_{ie}(x,t),$$

$$\tau_i \dot{V}_i(x,t) = V_i^{rest} - V_i(x,t) + \psi_{ei}(V_i(x,t))I_{ei}(x,t) + \psi_{ii}(V_i(x,t))I_{ii}(x,t),$$

$$\ddot{I}_{ee}(x,t) = -2\gamma_e \dot{I}_{ee}(x,t) - \gamma_e^2 I(x,t) + \Gamma_e(t)\gamma_e e(N_{ee}^{\beta} S(V_e(x,t) + p_{ee}(t))),$$

$$\ddot{I}_{ei}(x,t) = -2\gamma_e \dot{I}_{ei}(x,t) - \gamma_e^2 I_{ei}(x,t) + \Gamma_e(t)\gamma_e e(N_{ei}^{\beta} S(V_e(x,t) + p_{ei}(t))),$$

$$\ddot{I}_{ie}(x,t) = -(\gamma_i + \tilde{\gamma}_i)\dot{I}_{ie}(x,t) - \gamma_i \tilde{\gamma}_i I_{ie}(x,t) + \Gamma_i(t)\tilde{\gamma}_i e^{\gamma_i / \gamma_i^0}(N_{ie}^{\beta} S(V_i(x,t))), \quad (11)$$

$$\ddot{I}_{ii}(x,t) = -(\gamma_i + \tilde{\gamma}_i)\dot{I}_{ii}(x,t) - \gamma_i \tilde{\gamma}_i I_{ii}(x,t) + \Gamma_i(t)\tilde{\gamma}_i e^{\gamma_i / \gamma_i^0}(N_{ii}^{\beta} S(V_i(x,t))),$$

$$\dot{\Gamma}_e(t) = \frac{\Gamma_e^{rest} - \Gamma_e(t))}{\tau_e^{rec}} - p_e^{dep} S(V_e(x,t))\Gamma_e(t),$$

$$\dot{\Gamma}_i(t) = \frac{\Gamma_i^{rest} - \Gamma_i(t))}{\tau_i^{rec}} - p_i^{dep} S(V_i(x,t))\Gamma_i(t),$$

$$\psi_{lk}(V_k(x,t)) = \frac{[V_{lk}^{eq} - V_k(x,t)]}{|\, V_{lk}^{eq} - V_{x,k}^{r} \,|}, \quad k = e, i; \quad l = e, i\,.$$

2.3 Particle-filter-based parameter optimization method

In order to verify that the proposed model is able to match some characteristics of EEGs in AHE patients (AHE-EEGs), we developed a procedure for tuning the model parameter values. Therefore, with the constructed AHE-CM, this subsection introduces a model parameter optimization method based on particle filtering (PF-POM), which aims to help the model reproduce a key feature of clinical AHE-EEGs, namely the distribution of inter-TPW intervals (ITIs).

First, we describe the feature that we extract from AHE-EEGs. Triphasic waves (TPWs), also known as generalized periodic discharges, are a common pattern of brain activity in AHE-EEGs, consisting of epileptiform discharges repeating at relatively regular intervals. Fig. 3 (a) illustrates a 30s EEG segment recorded from a patient with AHE. The pink columns correspond to TPWs annotated by a semi-automatic annotation tool, Neurobroswer [42]. The rate at which specified events occur (i.e. frequency) is of interest clinically, because the patterns of periodic discharges that occur at higher frequencies are believed to be potentially harmful to patients and may warrant treatment with antiseizure drugs [43]. The intervals between consecutive TPWs can be used to characterize the occurring rate of TPWs: the rate is the inverse of the interval between TPWs. Given K TPWs in an AHE-EEG signal S, we can obtain a sequence of inter-TPWs intervals, denoted $\mathcal{I} = \{I_1, I_2, \cdots, I_{K-1}\}$, where I_k represents the interval (in seconds) between the kth and the $(k+1)$th TPWs. Then

the frequency histogram of $\mathcal{I}$ with M equally sized bins is defined as the extracted feature, denoted by

$$\mathbf{F}_1 = (P_1, P_2, \cdots, P_M) \tag{12}$$

where P_i denotes the probability of $\mathcal{I}$ in the ith bin. Fig. 3 (b) shows the frequency histogram of ITIs from the EEG of Fig. 3 (a).

In the following, we present the model parameter optimization method based on particle filtering (PF-POM) to match the extracted feature $\mathbf{F_1}$. Let S be an AHE-EEG signal and $V(\Theta)$ be the output of AHE-CM given the parameter vector Θ. Denote by $\mathbf{F_1}$ (**S**), $\mathbf{F_1}$ (**V**) the corresponding extracted feature vectors, We then define the fitness function in terms of $\mathbf{F_1}$ as follows:

$$L = \frac{1}{\sqrt{2\pi\sigma}} e^{-\frac{d^2}{2\sigma}} \tag{13}$$

where d represents the Bhattacharyya distance between $\mathbf{F_1}$ (**S**) and $\mathbf{F_1}$ (**V**) [44]. Next, we apply particle filtering (PF) [45] to find the optimal solution Θ^* of the optimization problem

$$\max_{\Theta} L\,. \tag{14}$$

Next, suppose that there are N particles in the PF (that is, $\Theta_1, \ldots, \Theta_N$), then we define the measurement at the kth iteration as

$$C_k = \log\left(\sum_{n=1}^{N} L(\Theta_n)\right), \tag{15}$$

and apply

$$| C_{k+1} - C_k | < \epsilon \tag{16}$$

as the stopping criterion. Here, ϵ is a given threshold. Furthermore, in our proposed method, all the parameters are initialized based on a uniform distribution in a large range since there is no prior knowledge. Therefore, a large amount of particles have to be supposed in PF, and hence, the computation cost becomes huge. Under such situation, we propose an improved approach to initialize parameter vector Θ so as to improve the efficiency of PF. Specifically, the parameter space is first separated into a number of sub-spaces, and one sub-space is selected on which the feature of model output is close enough to the feature of given EEG signal. Then all the parameters are initialized on the selected sub-space. With this approach, a much smaller number of particles is needed in the optimization.

The whole procedure of PF-POM procedure is illustrated in Fig. 4.

3 Experiments and results

This section explores the behaviors of our proposed model AHE-CM in 7 AHE patients.

3.1 AHE-EEG Data

The patients whose data were analyzed in this study were hospitalized at the Massachusetts General Hospital (MGH), and were encephalopathic during the EEG recordings. We selected 30-min scalp EEGs from seven AHE patients. These were selected from longer recordings to be relatively free of non-physiological artifacts. Moreover, they were chosen to coincide with times of maximal alertness. That is, as part of routine medical care, the EEG technologist stimulated each patient in attempt to ensure the patient was as awake as possible (although TPW EEG patterns are not compatible with normal levels of consciousness, i.e. these patients were all encephalopathic). Each of EEG segment contains 18 channels with a sampling rate of 128Hz. Details of AHE-EEGs are shown in Table 1, including gender, age and diagnosis. In our simulation, 0.5Hz high-pass and 60Hz notch filters are applied to de-noise the data before further analysis. All triphasic waves in each AHE-EEG were annotated manually in NeuroBroswer. Of note, TPWs are generally synchronous between hemispheres, and to a good approximation appear in all channels simultaneously. Therefore in annotating the timing of TPWs, we assigned a single time to each TPW across all channels.

3.2 Performance verification

In this subsection, we study the behaviours of our AHE-CM in response to changes in key parameters. We then present results of tuning the AHE-CM parameters using PF-POM to model the observed periodicity in AHE EEGs.

B1) Performance verification of three added mechanisms—Here we study model behaviors in response to changes of key parameters, and illustrate the effects of three extra mechanisms added to the Liley model. The four parameters τ_e^{rec}, τ_i^{rec}, F_{am}, γ_i, which are employed in the three mechanisms are considered the key parameters in the proposed AHE-CM. All other parameters in the model are set to their nominal values in Liley et al. [46], summarized in Table 2. The external input p_{ee} is generated randomly based following prior literature, by sampling from a Gaussian distribution with mean $3460s^{-1}$ and standard deviation $1000s^{-1}$; p_{ei} is constant ($5070s^{-1}$) [23]. We first focus on studying qualitatively what kind of model outputs are produced by different combination of key parameters. In all simulations, EEG signals of 50s duration were generated; the first 10s were ignored to exclude transient effects. The Matlab code used for the model simulations is provided in https://github.com/jill-Song/AHE-code.

The 7 types of simulated signals of AHE-CM are categorized according to the mean value of the inter-TPWs intervals (M-ITIs) in the simulated EEG segment (shown in Table 3). In Fig. 5 (a), we define a contrast between the 7 types of model outputs and their labels. The model output with label 1 represents a “low voltage” pattern. Labels 2 to 7 exhibit periodic discharges of increasing frequencies. Fig. 5 (b) illustrates the results under 9 different parameter settings, where each pair (F_{am}, γ_i) is taken from (3, 1.5, 0.8) × (0.065, 0.032,

0.014). In each case, τ_e^{rec} varies from 500 to 20000 with step-size 100, and τ_i^{rec} varies from 250 to 2500 with step-size 50. That is, each graph depicts 195 × 45 labels of model outputs. From Fig.5 (b), it can be seen that higher frequency periodic discharges occur for larger values of (F_{am}, γ_i), and smaller frequency discharges occur in the plots in the right panels with lower values of these parameters. On the other hand, in a graph with fixed F_{am} and γ_i, the discharges increase in frequency (label numbers increase) as τ_e^{rec} decreases and as τ_i^{rec} increases. These trends emerges very clearly in "graph (3)" where almost all patterns/labels occur.

We next examine one special case (as shown in Fig. 6 (d)) in detail to illustrate the effects of adding three extra mechanisms added to the baseline Liley model. Fig. 6 illustrates the outputs of four different models, each with one of the additional mechanism added in. In Fig. 6 (a), the output of the baseline Liley model is shown, where all parameters are set to their nominal values (see Table 2). Fig. 6 (b) illustrates the output of Liley model with the first mechanism added, where the postsynaptic potential amplitude Γ is determined by Eq. (7) with $\Gamma_k^{rest} = 0.71(k \in \{e, i\})$, $\tau_e^{rec} = 6000$, $\tau_i^{rec} = 1000$. We see that periodic waves begin to appear. The periodicity becomes more evident in Fig. 6(c), as the second mechanism is added, that is, when Γ is determined by both (7) and (8); in this illustration $F_{am} = 0.8$. Finally, the output of AHE-CM is obtained by adding all of three mechanisms, shown in Fig. 6 (d). Here, except for the estimated value of Γ as mentioned above, the decay rate constant γ_i is further calculated by (10). Interestingly, although reproducing the morphology of TPWs was not a goal of our modeling work, the close up in Fig. 6(d) shows that the output of the AHE-CM does provide an approximation of the morphology of TPWs. Each of the three red dots in close up of the waveform corresponds to one of the three phases of a TPW.

B2) Performance verification of AHE-CM combining with PF-POM—Next, we verify the ability of the proposed PF-POM method to infer the parameters of AHE-CM. We do this in simulated EEGs (generated by the AHE-CM model), because for these we know the true values for the underlying parameters. These true values can be served as a ground truth.

For simplicity, we consider only two key parameters τ_e^{rec}, τ_i^{rec}. We set $F_{am} = 0.8$, $\gamma_i = 0.032$, and all other parameters are set to their be nominal values in Table 2. According to the mentioned previously, the ranges of τ_e^{rec} and τ_i^{rec} are suggested to be [500,20000]ms and [250, 2500]ms. We first divide the parameter space into 5 sub-spaces by segmenting the interval of τ_e^{rec} and keeping the interval of τ_i^{rec} whole (see Table 4). Given an AHE-EEG signal S, we calculate the sequence of inter-TPW intervals $\mathcal{I}(\mathcal{S})$ as well as its mean, denoted by $mean(\mathcal{I}(\mathcal{S}))$. The sub-space related to S is then selected according to the value of $mean(\mathcal{I}(\mathcal{S}))$ shown as in Table 4. With the selected sub-space, the total number of particles is set to be $N = 35$ in our simulations.

In our PF-POM, the feature $\mathbf{F_1}$ is defined to be the frequency of TPWs in AHE-EEGs. To illustrate this feature, Fig. 7 shows the frequency histogram of $\mathcal{I}$ with respect to two signals

(S_{fast} and S_{slow}) with different frequencies (fast and slow) of TPWs. In Fig. 7 (b), the frequency histogram of $\mathcal{I}(S_{fast})$ is left-skewed normal distribution toward lower inter-TPW intervals, reflecting the higher average frequency of simulated TPWs signal S_{fast}. By contrast, the histogram of $\mathcal{I}(S_{slow})$ are more uniformly distributed and are concentrated at higher inter-TPW intervals, reflecting the slower average rate of TPWs in S_{slow}.

We next verify the ability of PF-POM to estimate model parameters from simulated EEG data. Given parameters values $(\tau_e^{rec}, \tau_i^{rec}) = (1100, 600)$, the model output ("simulated EEG") is computed according to Eqs. (11). Applying the PF-POM yields estimates $(\tau_e^{rec})^*$ and $(\tau_i^{rec})^*$. Fig. 8 illustrates the results for 50 trials, where the mean and standard variation of them are shown. To further verify the performance of PF-POM, we compare model output with the true underlying parameters to the model output using the estimated parameter values. In Fig. 9, the red curve shows the original simulated EEG signal (labeled as "ground truth"), and the green curve shows the model output with the optimal values determined by PF-POM (here, one of the results in 50 trials is randomly selected to create the green curve and labeled as "simulated"). The comparison illustrates that effectiveness of the proposed PF-POM.

B3) Relation between features of AHE-EEGs and the mechanistic model of AHE—In this section, we focus on the relation between the frequency of TPWs in real AHE-EEGs and the mechanisms underlying AHE in our computational model. We have seen in Fig. 5 that variation in TPWs' rate depends mainly on τ_e^{rec} and τ_i^{rec}. Especially, when $F_{am} = 0.8$, $\gamma_i = 0.065$, the much more clear variation in all TPW patterns can be observed. Therefore in what follows, we use PF-POM to optimize only τ_e^{rec} and τ_i^{rec} ($F_{am} = 0.8$, $\gamma_i = 0.065$), in the AHE-CM, and leave the values of the other variables at their nominal values.

In our analysis of AHE-EEG data from patients, each signal is divided into 20s EEG segments. Then given each AHE-EEG segment, we use PF-POM to estimate the values τ_e^{rec}, τ_i^{rec} of an AHE-CM model that best match the data. We then use the estimated AHE-CM model generate a simulated EEG segment (i.e., output of AHE-CM). Table 5 shows the number of TPWs in AHE-EEGs (TA) and simulated EEGs (TS), the mean of ITIs in AHE-EEGs (MA) and simulated EEGs (MS), as well as the corresponding "errors" / differences. Comparing "No. of TPWs" in 30min-long AHE-EEGs and simulated EEGs, the maximum error is 0.0734 and the minimum error is 0.0322, obtained by $\frac{|TA - TS|}{TA}$. Moreover, the errors between "mean of ITIs" in AHE-EEGs and simulated EEGs, $|MA - MS|$, fall inside the range [0.01, 0.06]. We thus conclude that the simulated EEGs resulting from our proposed approach "AHE-CM + PF-POM" have similar properties to AHE-EEGs with respect to periodicity of TPWs. Fig. 10 illustrates a 20s AHE-EEG segment from "patient 1" and the simulated EEG segment from the corresponding AHE-CM model after parameter optimization. The pink columns correspond to the annotated TPWs. We observe that 30 TPWs are included in the AHE-EEG segment, whose mean of ITI is 0.6442 (Fig. 10(a)).

The model with estimated parameters produces 29 TPWs with mean ITI 0.6679 (Fig. 10(b)). These results suggest that optimizing τ_e^{rec} and τ_i^{rec} indeed is able to qualitatively match the periodic discharge behavior of real AHE EEGs.

We next focus on characterizing the relation between the rate of TPWs in AHE-EEGs and the mechanisms underlying AHE. From the above experimental results, we select 9 out of 90 segments for each patient (shown in the Supplementary material), and the corresponding mean IEI values and optimal parameter settings (τ_e^{rec}, τ_i^{rec}) estimated for each segment. In Fig. 11, 63 points (9 × 7) are marked whose position corresponds to the optimal parameters determined by PF-POM and whose value is the mean of its ITIs (M-ITIs). We observe that EEG segments having comparatively small values of M-ITIs (i.e. high frequency of TPWs) locate at the bottom right corner of the graph (corresponding to small τ_e^{rec} and large τ_i^{rec}), and EEG segments are located at the upper-left of the graph having comparatively high values of M-ITIs (corresponding to small τ_e^{rec} and large τ_i^{rec}).

These results are plausible from a physiological point of view. Here, parameters τ_e^{rec} and τ_i^{rec} represent the recovery times for excitatory and inhibitory activities respectively. Therefore, the less the value of τ_e^{rec} is, the more quickly recovery of excitatory activity will be, thus the faster the excitatory activity cam resume - leading to higher frequency discharges. Similarly, the excitatory activity can also recover more quickly if the value of τ_i^{rec} is larger. On the basis of the above analysis, we hypothesize that the discharge rate of TPWs in real AHE-EEGs is related to recovery times of excitatory and inhibitory neural populations.

4 Discussion

In this study we built a computational model that accounts, at least in part, for generalized periodic epileptiform discharges in the EEG of patients with acute hepatic encephalopathy (AHE), an EEG pattern known as “triphasic waves” (TPWs). Our model is based on the Liley model, augmented with three mathematically characterized mechanisms known to play a role in the encephalopathy that occurs in AHE, namely increased excitability, impaired synaptic transmission, and enhanced postsynaptic inhibition. We also proposed an approach to identify model parameter values that are able to quantitatively match a key characteristic of real EEGs in AHE patients, namely the periodicity of TPWs.

Generalized periodic discharges, including triphasic waves, also occur in contexts other than AHE. These include uremia, severe sepsis, baclofen toxicity, anoxic brain injyry, and other “toxic metabolic encephalopathies” [47,43,48]. However, with one exception, the underlying physiology / pathophysiology of most of these conditions is more poorly understood than AHE. The exception is hypoxic ischemic encephalopathy (HIE). HIE has been modeled previously by Rujiter et.al., using the same modified Liley model. Ruijter et al identified three key mechanisms in acute HIE captured by the modified Liley model, namely: short-term synaptic depression, potentiation of excitatory neurotransmission, and altered synaptic inhibition (due to effect of propofol) into the “Bursting liley model”. We can see that these

pathophysiological alterations are similar to the mechanisms that we have invoked for AHE: elevated neuronal excitability, impaired synaptic transmission secondary to reduced cellular bioenergetics and enhanced postsynaptic inhibition. Given the strong similarities between generalized periodic discharges in other forms of severe encephalopathy, we hypothesize that similar mechanisms will also be discovered to be in play in those conditions.

Note that the proposed model AHE-CM is a kind of mesoscopic model, which is a typical over-simplified method to characterize the brain discharge. And the AHE-EEGs applied in our work are recorded with the noninvasive electrodes placed along the scalp, where electrical potentials are smeared due to the existence of cerebrospinal fluid, skull and scalp, as well as contaminated due to a significant presence of environmental noise and artifacts. Under such situation, there must exist a big gap between the details of EEG waveforms in real AHE-EEGs and the model output themselves. Alternatively, our work accounts only for some, but not all, aspects of the EEG in patients with AHE. In particular, our aim was to account for certain properties of generalized periodic discharges seen in AHE, known as triphasic waves, specifically their frequency.

It is necessary to clarify that our model does not include spatial aspects of TPWs. In fact, we only simulated a single EEG channel. This is justified in part by the fact that EEG patterns in hepatic encephalopathy are typically spatially homogeneous. However, particular phenomena, such as bilateral synchronization of TPWs, anterior-posterior lag or gradient are not explained by our model. In order to illustrate these spatial characteristics of TPWs, the network-level neural computational models need to be constructed, which represent the interaction of multiple neural populations located in different cortical areas. Therefore, in the future study, the network-level neural computational modeling is a research frontier we are going to follow. It may not only be helpful to simulate morphology of TPWs similar to the real TPWs, but also may provide novel insight for understanding the arising of TPWs in AHE-EEGs.

5 Conclusion

The computational model proposed herein provides a mechanistic account, albeit partial, of the generalized periodic discharges seen in AHE, known as triphasic waves. Our model is based on three modifications of the well-studied Liley model that are believed central to brain dysfunction in AHE: increased neuronal excitability, impaired synaptic transmission, and enhanced post-synaptic inhibition. Then we introduced a model parameter optimization method based on particle filtering (PF-POM), by combining the feature extracted from AHE-EEGs, namely the distribution of inter-TPW intervals. Finally, we applied the proposed approach to EEG data from AHE patients, performing the following investigations: (1) verification of the ability of the three mechanisms added to the Liley model to produce periodic discharges of various frequencies; (2) performance of the ability of the PF-POM method to estimate the parameters of simulated EEGs generated by AHE-CMs; and (3) investigation of how features of real AHE EEGs relate to mechanistic processes and parameter values in the computational model. By combining model-driven and data-driven approaches, our approach not only reproduces important aspects of the EEG, but also suggests mechanisms underlying variation in EEG patterns in AHE. In particular, our model

provides a mechanistic explanation for why more severe AHE results in TPWs of higher frequency.

Supplementary Material

Refer to Web version on PubMed Central for supplementary material.

Acknowledgements

This work was supported by the National Natural Science Foundation of China under Grant 61473223 the Innovative Talents Promotion Plan of Shaanxi Province under Grant 2018TD-016, and the Foundation for the National Institutes of Health of United States under Grants 1K23NS090900, 1R01NS102190, 1R01NS102574, 1R01NS107291.

References

1. Amodio P, Del Piccolo F, Pettenò E, Mapelli D, Angeli P, Iemmolo R, Muraca M, Musto C, Gerunda G, Rizzo C, et al., Journal of hepatology 35(1), 37 (2001) [PubMed: 11495040]
2. D'amico G, Morabito A, Pagliaro L, Marubini E, et al., Digestive diseases and sciences 31(5), 468 (1986) [PubMed: 3009109]
3. Wijdicks EF, New England Journal of Medicine 375(17), 1660 (2016) [PubMed: 27783916]
4. Hirsch L, LaRoche S, Gaspard N, Gerard E, Svoronos A, Herman S, Mani R, Arif H, Jette N, Minazad Y, et al., Journal of clinical neurophysiology 30(1), 1 (2013) [PubMed: 23377439]
5. Agrawal S, Umapathy S, Dhiman RK, Journal of clinical and experimental hepatology 5, S42 (2015) [PubMed: 26041957]
6. Shayegh F, Bellanger JJ, Sadri S, Amirfattahi R, Ansari-Asl K, Senhadji L, Journal of medical signals and sensors 3(1), 2 (2013) [PubMed: 24083132]
7. Wilson HR, Cowan JD, Biophysical journal 12(1), 1 (1972) [PubMed: 4332108]
8. Beurle RL, Trans. Roy. Soc. (Lond) B 240, 55 (1956)
9. Nunez PL, Mathematical Biosciences 21(3-4), 279 (1974)
10. Hutt A, Buhry L, Journal of computational neuroscience 37(3), 417 (2014) [PubMed: 24976146]
11. Fröhlich F, Jezernik S, Journal of computational neuroscience 17(2), 165 (2004) [PubMed: 15306738]
12. Jansen BH, Zouridakis G, Brandt ME, Biol. Cybern 68, 275 (1993) [PubMed: 8452897]
13. Jansen BH, Rit VG, Biol. Cybern 73, 357 (1995) [PubMed: 7578475]
14. Wendling F, Bartolomei F, Chauvel P, Biol. Cybern 83, 367 (2000) [PubMed: 11039701]
15. Babajani-Feremi, Soltanian-Zadeh H, NeuroImage 52, 793811 (2010)
16. Zavaglia M, Astolfi L, Babiloni F, Ursino M, Journal of Neuroscience Methods 157, 317329 (2006)
17. RJ M, SJ K, KE S, RB R, J D, KJ F, Neuroimage 37, 706 (2007) [PubMed: 17632015]
18. Zandt BJ, Visser S, van Putten MJ, ten Haken B, Journal of computational neuroscience 37(3), 549 (2014) [PubMed: 25131270]
19. Rotterdam AV, Silva FHLD, Ende JVD, Viergever MA, Hermans AJ, Bulletin of Mathematical Biology 44(2), 283 (1982) [PubMed: 7074252]
20. Freeman WJ, Biological Cybernetics 56(2-3), 139 (1987) [PubMed: 3593783]
21. Liley DT, Spatiotemporal models in biological and artificial systems. Amsterdam: IOS Press pp. 89–96 (1997)
22. Liley DT, Cadusch PJ, Wright JJ, Neurocomputing 26, 795 (1999)
23. Ruijter BJ, Hofmeijer J, Meijer HGE, van Putten MJAM, Clinical neurophysiology 128(9), 1682 (2017) [PubMed: 28753456]
24. Ermentrout B, Neural Computation 6(4), 679 (1994)

25. Kosenko E, Kaminsky Y, Grau E, Miñana MD, Marcaida G, Grisolía S, Felipo V, Journal of neurochemistry 63(6), 2172 (1994) [PubMed: 7964737]
26. Dhanda S, Sunkaria A, Halder A, Sandhir R, Metabolic brain disease 33(1), 209 (2018) [PubMed: 29138968]
27. Monfort P, Kosenko E, Erceg S, Canales JJ, Felipo V, Neurochemistry international 41(2-3), 95 (2002) [PubMed: 12020609]
28. Back T, Nedergaard M, Ginsberg M, Cerebrovascular Disease: Pathophysiology, Diagnosis and Management. Malden, Mass: Blackwell Science pp. 276–286 (1998)
29. Weiss N, Saint Hilaire PB, Colsch B, Isnard F, Attala S, Schaefer A, del Mar Amador M, Rudler M, Lamari F, Sedel F, et al., Journal of hepatology 65(6), 1120 (2016) [PubMed: 27520878]
30. Marcaida G, Felipo V, Hermenegildo C, Miñana MD, Grisolia S, FEBS letters 296(1), 67 (1992) [PubMed: 1346118]
31. Knecht K, Michalak A, Rose C, Rothstein JD, Butterworth RF, Neuroscience letters 229(3), 201 (1997) [PubMed: 9237493]
32. Fauci AS, et al., Harrison's principles of internal medicine, vol. 2 (Mcgraw-hill New York, 1998)
33. Saija A, Princi P, Lanza M, Scalese M, Aramnejad E, De Sarro A, Life sciences 56(10), 775 (1995) [PubMed: 7885193]
34. Butterworth RF, The Journal of steroid biochemistry and molecular biology 160, 94 (2016) [PubMed: 26589093]
35. Ferenci P, in Assessment and Management of Hepatobiliary Disease (Springer, 1987), pp. 431–435
36. Barbaro G, Di Lorenzo G, Soldini M, Giancaspro G, Bellomo G, Belloni G, Grisorio B, Annese M, Bacca D, Francavilla R, et al., Hepatology 28(2), 374 (1998) [PubMed: 9695999]
37. Bojak I, Stoyanov ZV, Liley DT, Frontiers in systems neuroscience 9, 18 (2015) [PubMed: 25767438]
38. Bojak I, Liley D, Physical Review E 71(4), 041902 (2005)
39. Tsodyks MV, Markram H, Proceedings of the national academy of sciences 94(2), 719 (1997)
40. Khazipov R, Congar P, Ben-Ari Y, Journal of neurophysiology 74(5), 2138 (1995) [PubMed: 8592202]
41. Izumi Y, Svrakic N, ODell K, Zorumski CF, Neuroscience 233, 166 (2013) [PubMed: 23276672]
42. Jing J, Dauwels J, Rakthanmanon T, Keogh E, Cash S, Westover M, Journal of neuroscience methods 274, 179 (2016) [PubMed: 26944098]
43. O'Rourke D, Chen PM, Gaspard N, Foreman B, McClain L, Karakis I, Mahulikar A, Westover MB, Neurocritical care 24(2), 233 (2016) [PubMed: 26013921]
44. Kailath T, IEEE transactions on communication technology 15(1), 52 (1967)
45. Salmond D, Birch H, in American Control Conference, 2001 Proceedings of the 2001, vol. 5 (IEEE, 2001), vol. 5, pp. 3755–3760
46. Liley DT, Bojak I, Journal of Clinical Neurophysiology 22(5), 300 (2005) [PubMed: 16357635]
47. Kaplan PW, Sutter R, Journal of clinical neurophysiology 32(5), 401 (2015) [PubMed: 26426768]
48. Foreman B, Mahulikar A, Tadi P, Claassen J, Szaflarski J, Halford JJ, Dean BC, Kaplan PW, Hirsch LJ, LaRoche S, et al., Clinical Neurophysiology 127(2), 1073 (2016) [PubMed: 26294138]

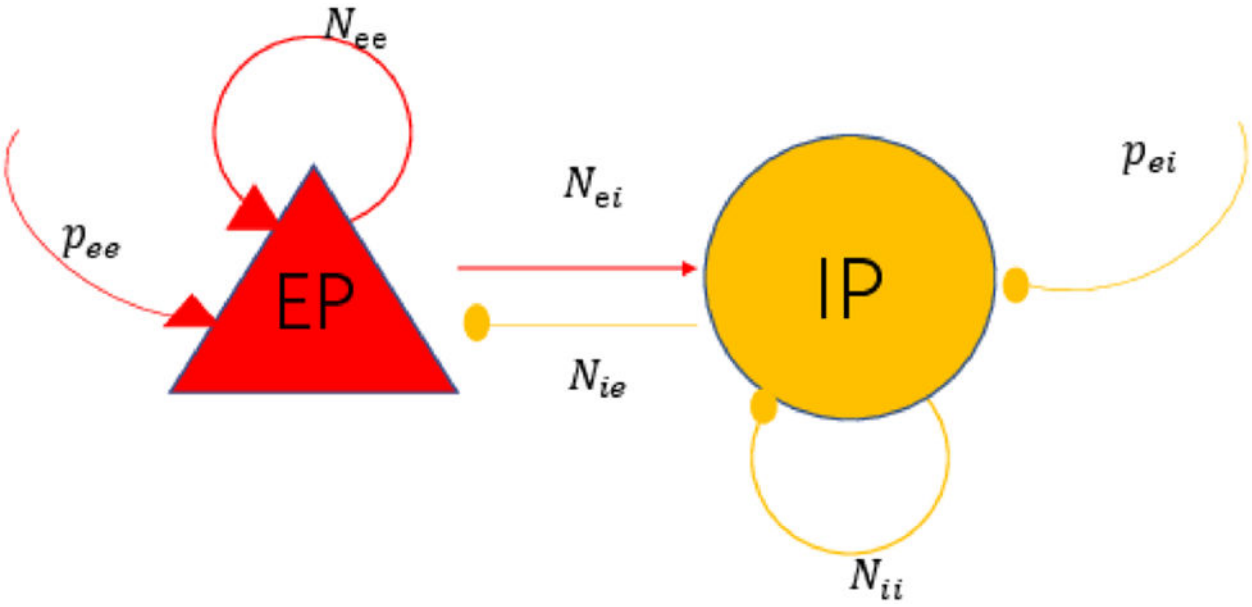

Fig. 1.
Sketch of Liley model.

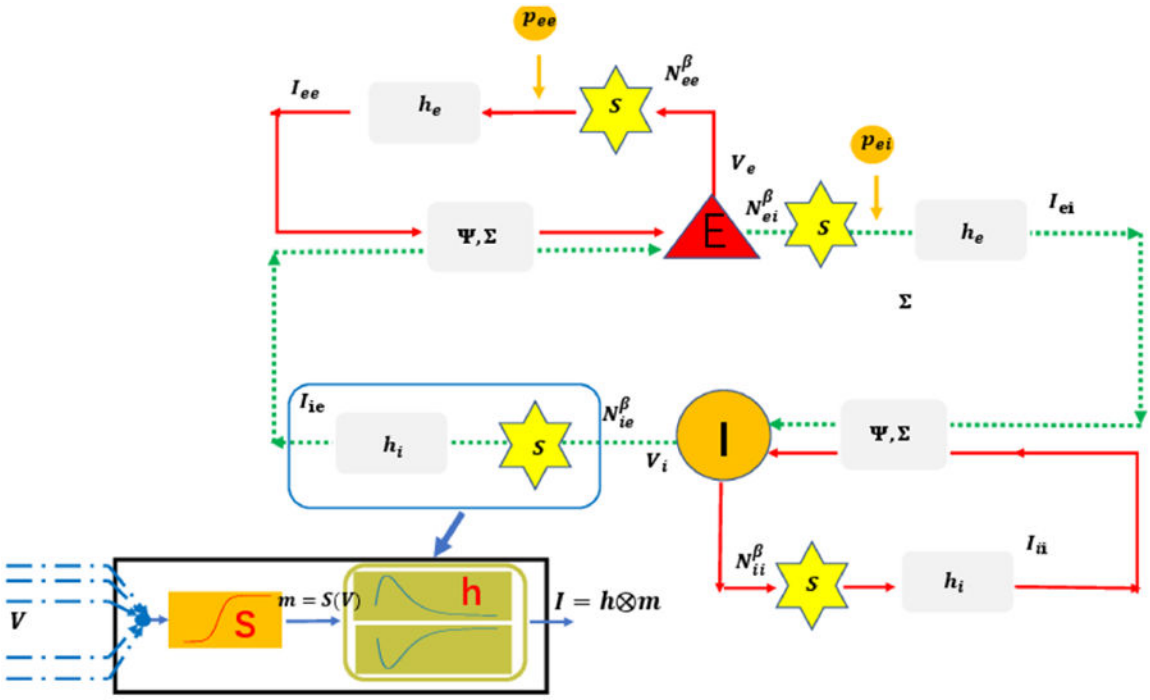

Fig. 2.
The detailed transformation of electrical activities in Liley model.

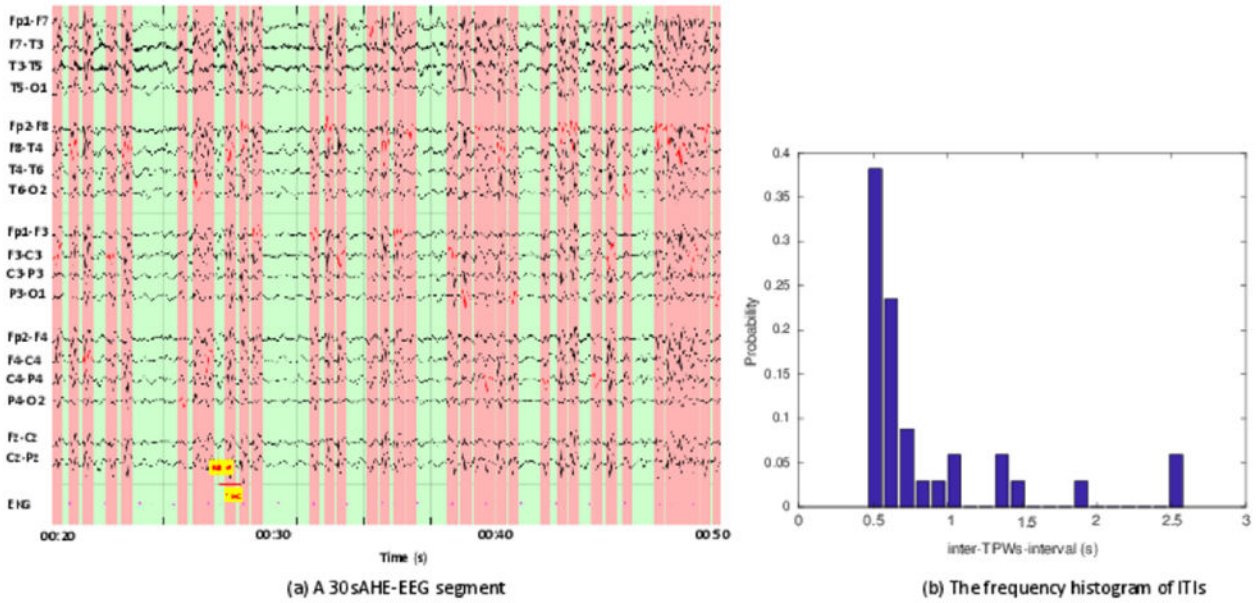

Fig. 3.
An AHE-EEG segment and extracted features.

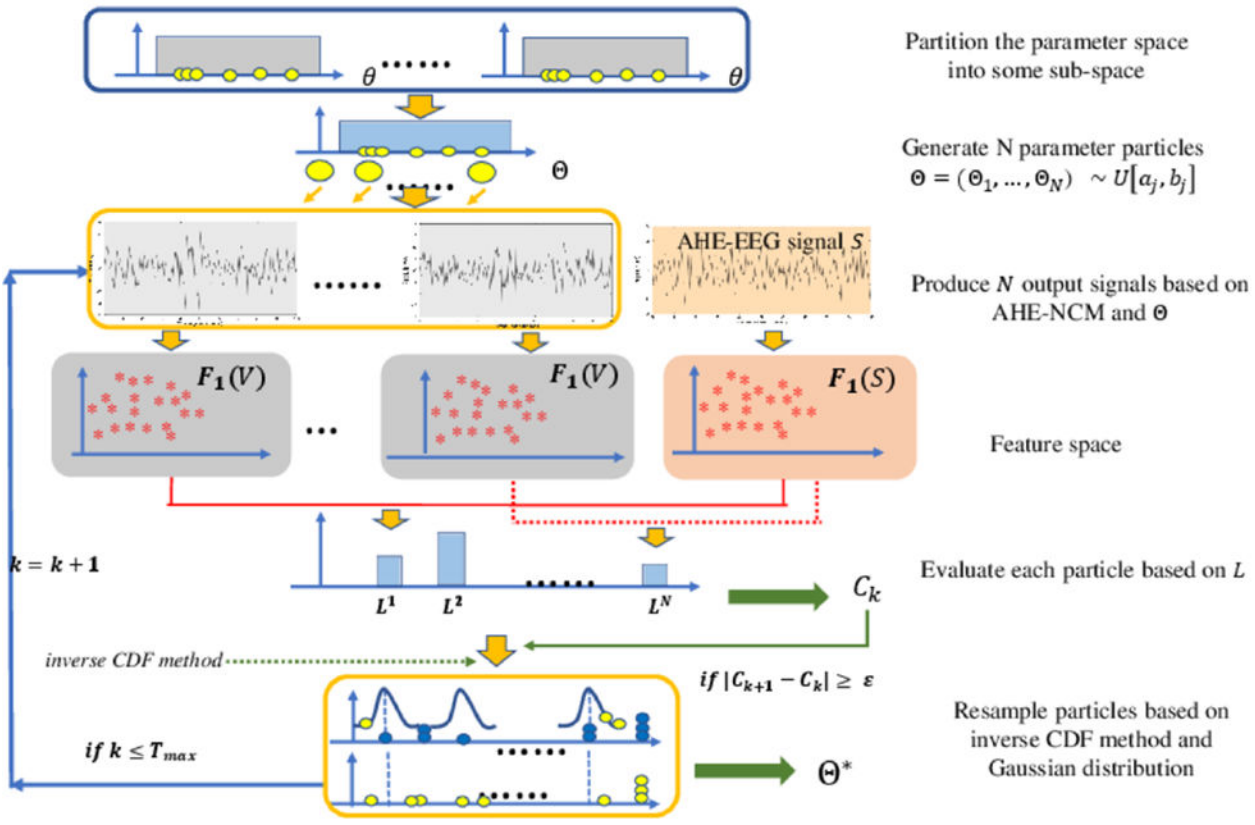

Fig. 4.
The procedure of particle-filter-based parameter estimation method.

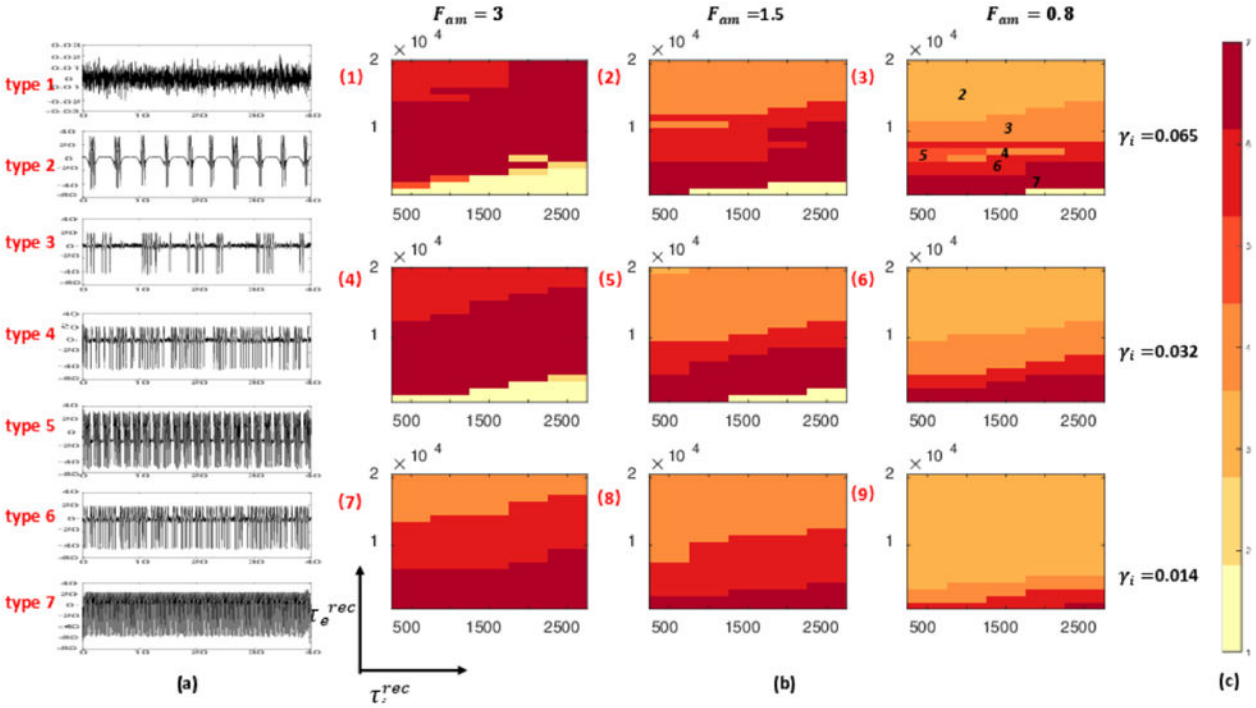

Fig. 5.

(a) A contrast between 7 types of model outputs and their labels; (b) the distribution of model output labels under 9 different cases where (F_{am}, γ_i) ∈ (3, 1.5, 0.8) × (0.065, 0.032, 0.014) (here, τ_e^{rec}(500:100:20000), τ_i^{rec}(250:50:2500); (c) color bar of 7 types of model outputs.

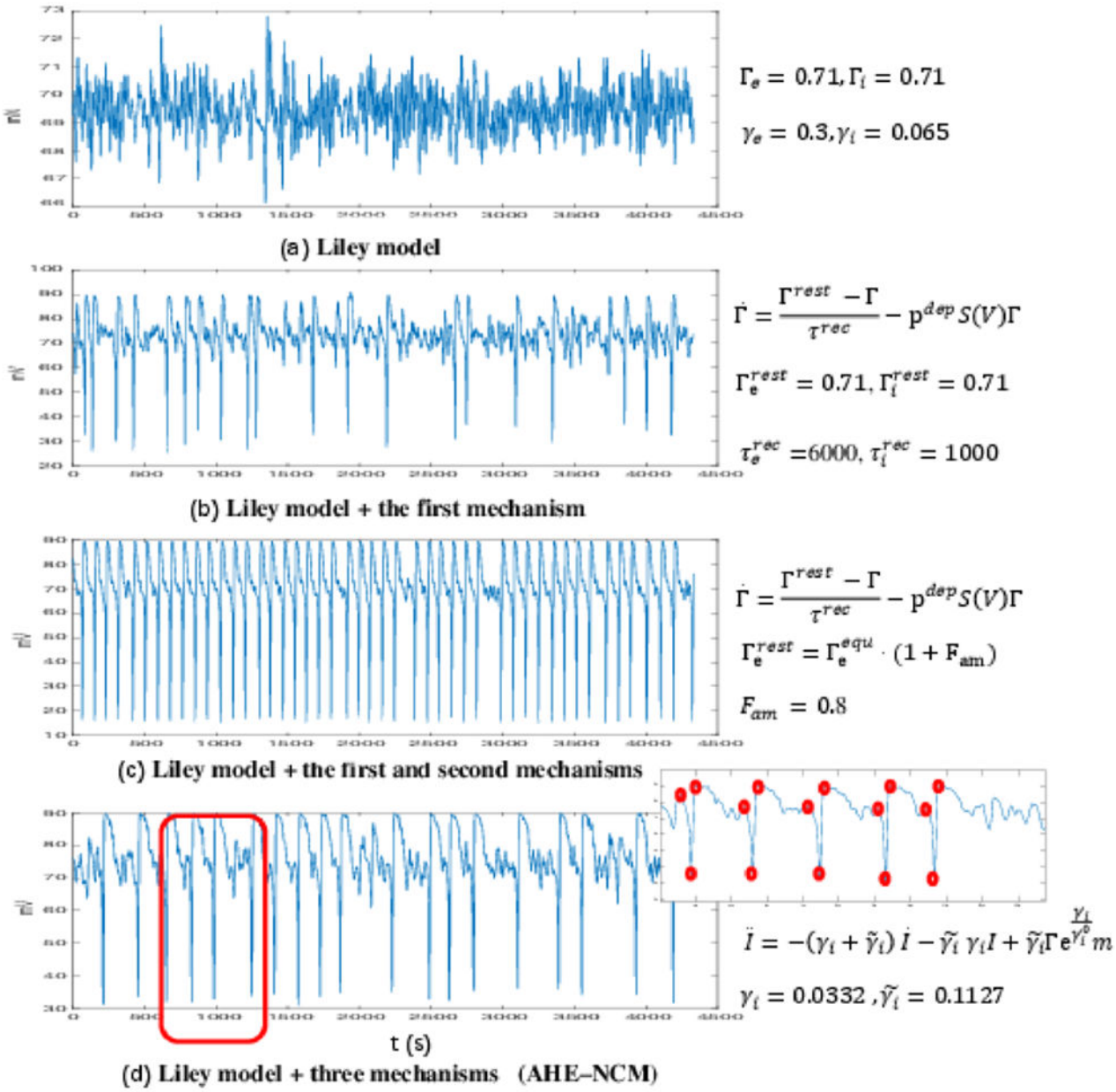

Fig. 6.
The effects of adding three extra mechanisms added to the baseline Liley model.

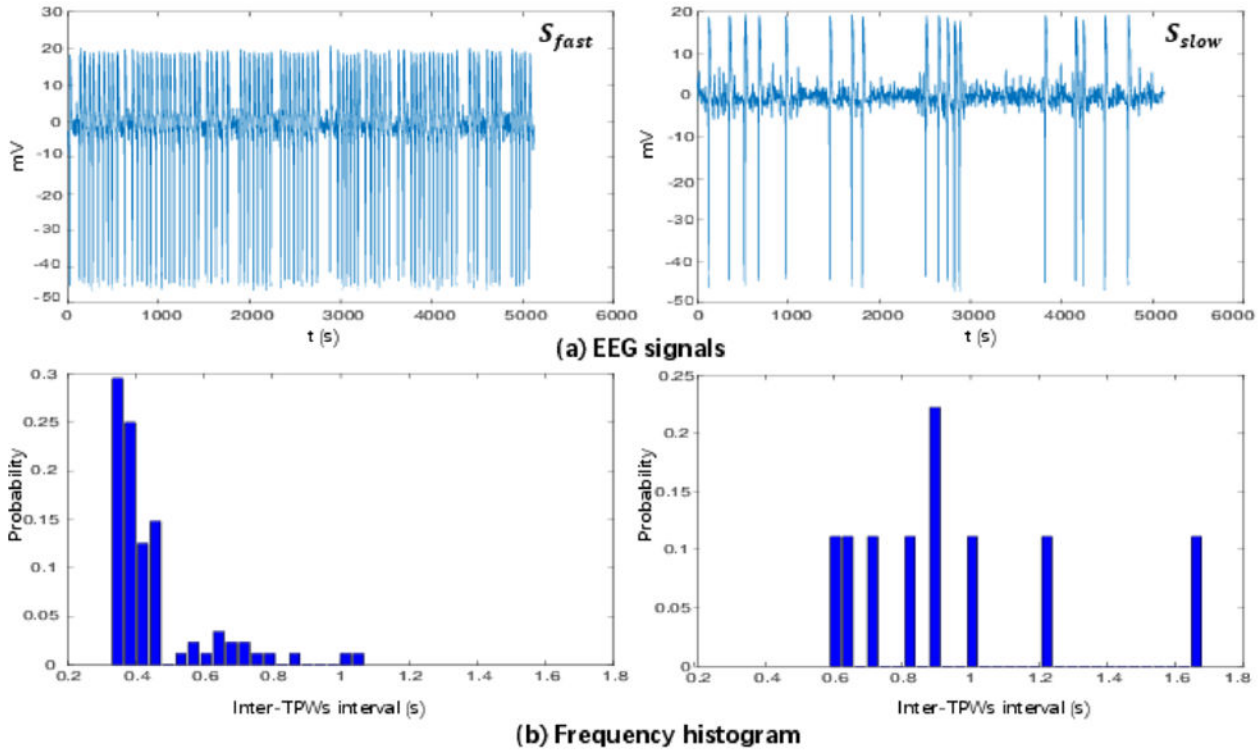

Fig. 7.

The feature $\mathbf{F_1}$ of two AHE-EEG signals (S_{fast} and S_{slow}).

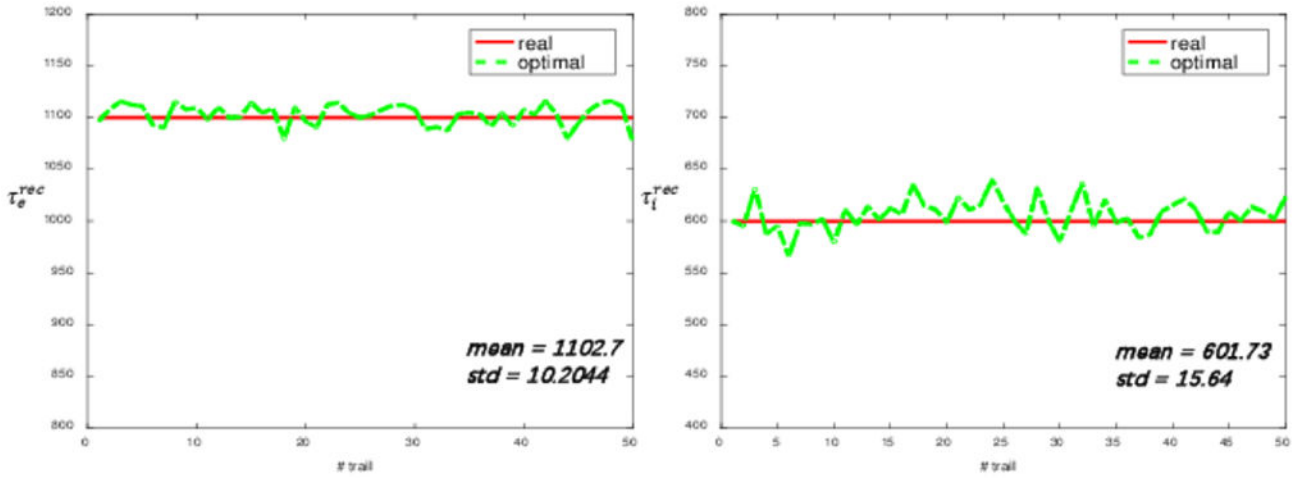

Fig. 8.

The optimized values of τ_e^{rec} and τ_i^{rec} in 50 trails.

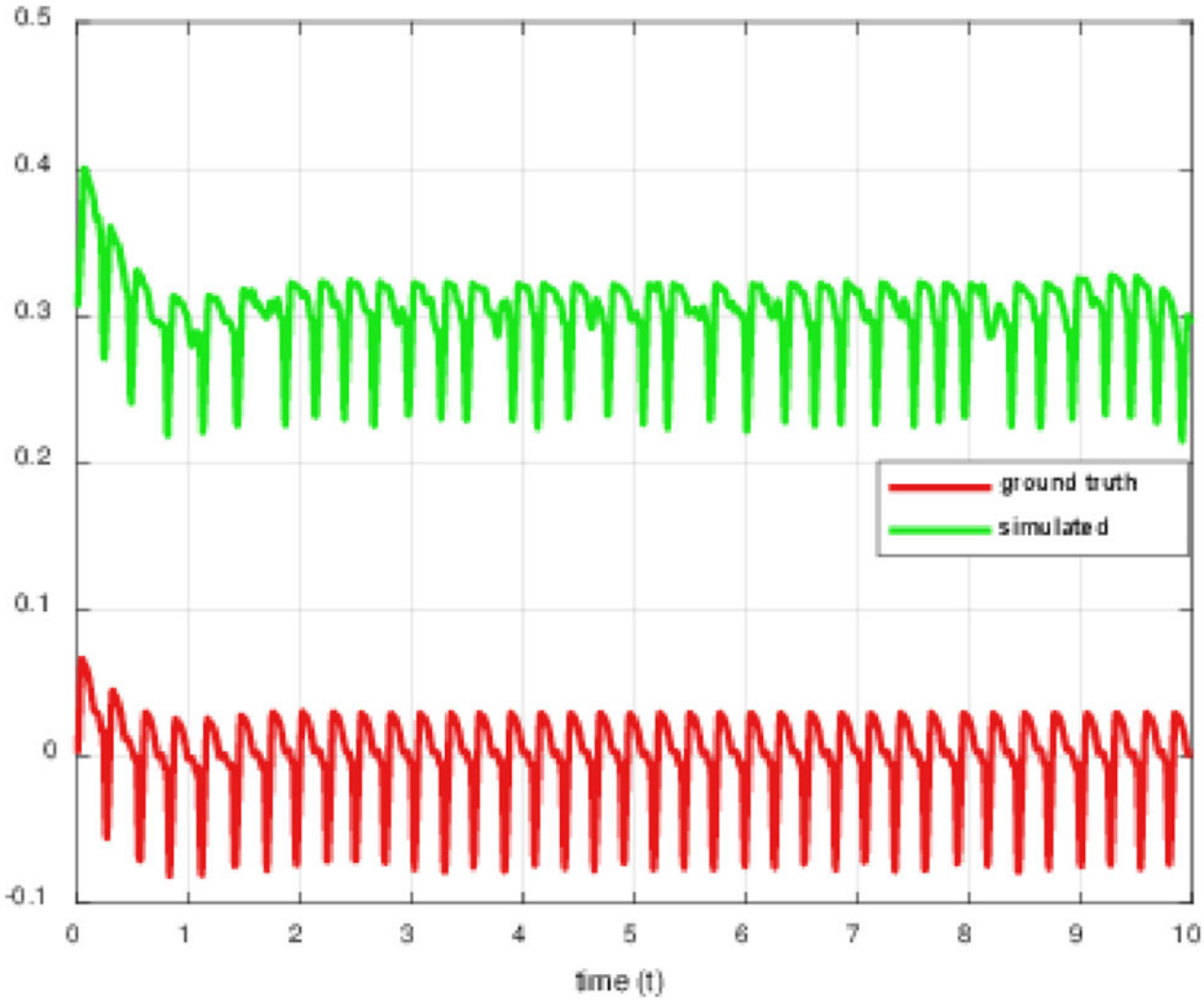

Fig. 9.

Comparison between the original simulated EEG signal (labeled as “ground truth”) and the model output with the optimal values determined by PF-POM (labeled as “simulated”)

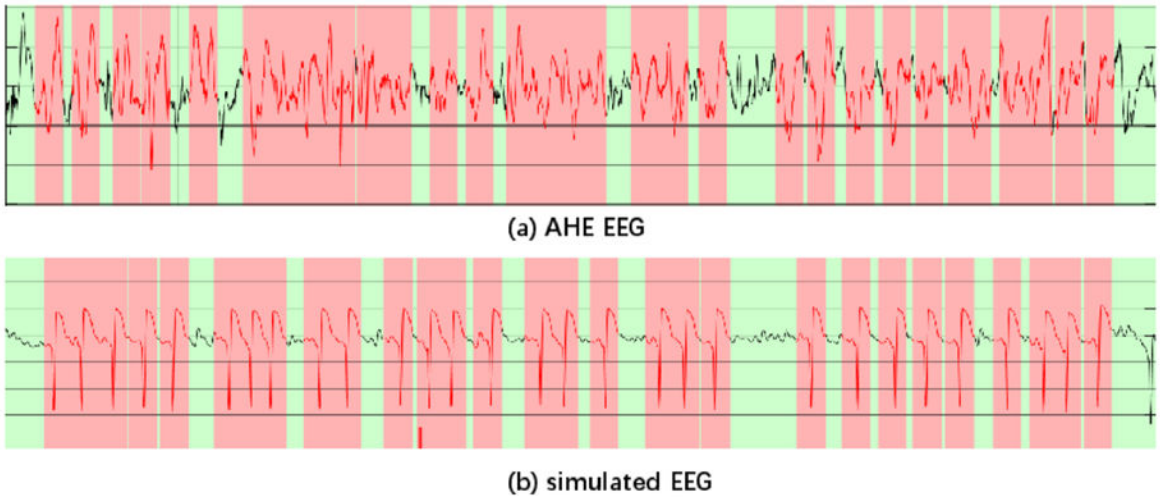

Fig. 10.

An AHE-EEG segment (20s) from “patient 1” and the simulated EEG segment by the proposed approach “AHE-NCM + PF-POM”

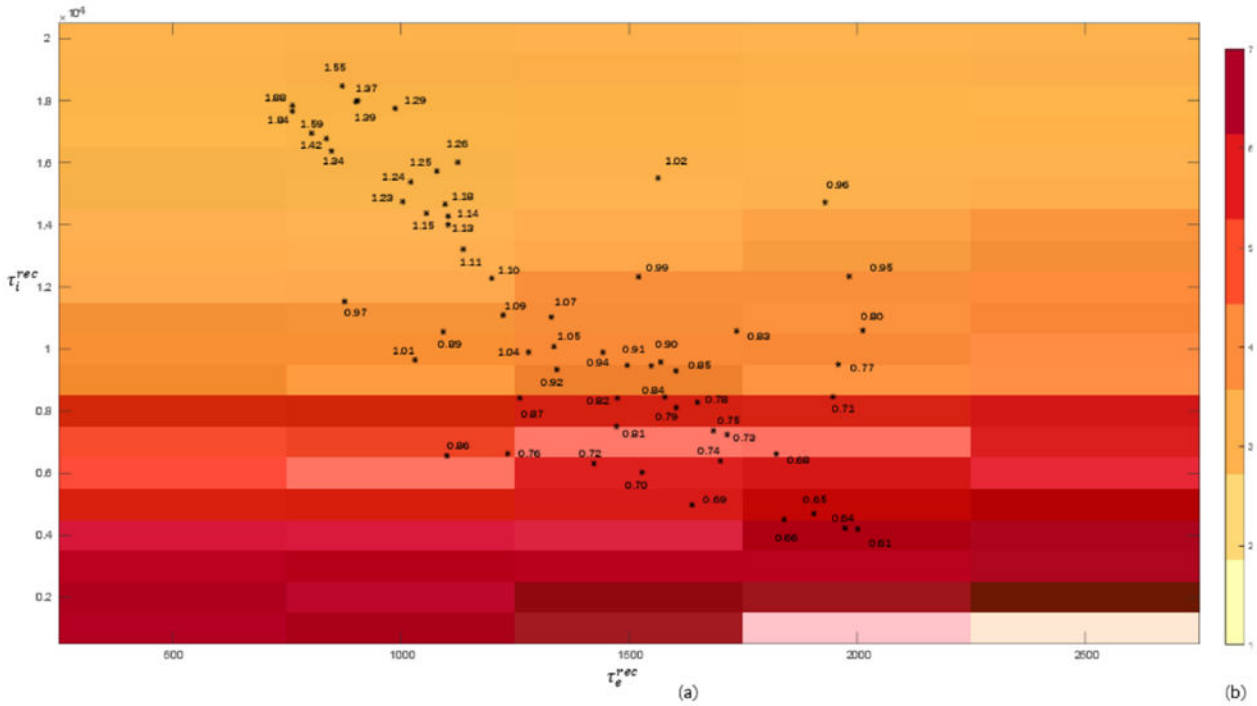

Fig. 11.

a) The distribution of mean of ITIs in a parameter space $\tau_e^{rec} \times \tau_i^{rec}$; b) color bar of 7 types of model outputs.

Table 1

The details of AHE-EEGs

patients	gender	age	diagnosis information
1	M	73	4,11
2	F	80	4,11
3	M	69	4,11
4	M	61	4,11
5	M	77	4,11
6	F	64	4,11
7	F	82	4,11

Liver disorders =4; Toxic metabolic encephalopathy=11

Table 2

The parameters and their nominal values in AHE-NCM

Parameter	Nominal value	Unit
V_e^r, V_i^r	−70	mv
Γ_i^{rest}	0.71	mV
V_{ee}^{eq}, V_{ei}^{eq}	45	mv
V_{ie}^{eq}, V_{ii}^{eq}	−90	mv
τ_e	94	ms
τ_i	42	ms
V_0	−50	mv
σ	5	mv
γ_e	300	s^{-1}
γ_i^0	65	s^{-1}
Q^{max}	500	s^{-1}
$N_{ee}^{\beta}, N_{ei}^{\beta}$	3000	/
$N_{ie}^{\beta}, N_{ii}^{\beta}$	500	/
p_e^{dep}, p_i^{dep}	0.003	/

Table 3

Determination of labels

M-ITIs	**≥2.5**	**(1.5 2.5]**	**(0.7 1.5]**	**(0.4 0.7]**	**(0.2 0.4]**	**≤ 0.2**
Label	2	3	4	5	6	7

Table 4

Division and selection rule of subspaces

Parameters $(\tau_e^{rec}, \tau_i^{rec})$ **(s)**	**[0.5, 6] × [0.25, 2.5]**	**[6, 8] × [0.25, 2.5]**	**[8, 11] × [0.25, 2.5]**	**[11, 15] × [0.25, 2.5]**	**[15, 20] × [0.25, 2.5]**
Sub-spaces	1	2	3	4	5
Mean($\mathcal{F}(\mathcal{S})$) (s)	≤ 0.5	(0.5, 0.7]	(0.7, 0.9]	(0.9, 1.1]	> 1.1

Table 5

Comparison results between AHE-EEG and simulated EEG

Patient	AHE-EEG		simulated EEG		error	
	No. of TPWs (TA)	mean of ITIs (MA)	No. of TPWs (TS)	mean of ITIs (MS)	No. of TPWs	mean of ITIs
1	1710	0.9065	1765	0.8824	0.0322	0.0241
2	1924	0.9343	1816	0.9539	0.0561	0.0196
3	1705	1.0557	1799	1.0126	0.0551	0.0431
4	1701	1.0583	1621	1.1145	0.0471	0.0562
5	1374	1.3093	1466	1.2642	0.0669	0.0451
6	1639	1.0981	1522	1.1568	0.0714	0.0587
7	1513	1.1888	1402	1.2159	0.0734	0.0271